Chemical Science

ROYAL SOCIETY OF CHEMISTRY

EDGE ARTICLE

View Article Online
View Journal

Cite this: DOI: 10.1039/d6sc02775j

All publication charges for this article have been paid for by the Royal Society of Chemistry

Isomeric model molecules: understanding and regulating the emission nature of multiple-resonance thermally activated delayed fluorescence

Xinliang Cai,†[ab] Rajat Walia,†[c] Weixiong Guo,[d] Yexuan Pu,[b] Jinbei Wei,*[a] Xian-Kai Chen*[c] and Yue Wang*[b]

Received 3rd April 2026
Accepted 1st June 2026

DOI: 10.1039/d6sc02775j

rsc.li/chemical-science

Multi-resonance thermally activated delayed fluorescence (MR-TADF) emitters exhibit high photoluminescence quantum yields and exceptional color purity, driving significant interest in high-performance organic light-emitting diode (OLED) applications. Current strategies for constructing full-color MR-TADF emitters rely on intricate structural designs to regulate emission wavelengths, yet overlook critical photophysical parameters (such as emission maximum, excited-state lifetime, and so on) and obscure fundamental structure–property relationships, impeding precise control over photophysical behaviours. To address this issue, this study adopts a unique isomeric design strategy to reveal the basic emission properties of MR-TADF molecules. By systematically probing subtle connectivity differences within conserved mono-boron and dual-boron-based multi-resonant skeletons, the chemical bonding pattern dependent emission property was investigated. The critical factors affecting emission wavelength and excited-state lifetime have been uncovered. The detailed theoretical analyses provided a reasonable explanation for these results. This study establishes a molecular design strategy for precise optimization of emission properties, offering deep insights to facilitate the development of high-performance MR-TADF materials. Moreover, the exceptional device performance of compounds *v*-DABNA-Cz and *x*-DABNA with high efficiency and satisfactory color purity demonstrates the practicality and significance of the developed method.

Introduction

Multi-resonance thermally activated delayed fluorescence (MR-TADF) emitters based on organoboron–nitrogen (B/N) containing molecules represent a significant advancement in photophysical characteristics, offering exceptional promise for next-generation organic light-emitting diodes (OLEDs).[1–5] The unique frontier molecular orbital (FMO) distributions arise from a multiple resonance (MR) effect in the rigid B/N-embedded polycyclic frameworks, resulting in a short-range charge transfer (SRCT) excited state that enables both high photoluminescence quantum yields (Φ_{PL}s ≥ 90%) and remarkably narrow band emission (full width at half maximum: FWHM ≤ 30 nm).[6–8] These unique features confer a distinct advantage on MR-TADF emitters over spatially separated donor–acceptor (D–A) type TADF emitters, which inherently suffer from broad emission bands due to the long-range charge transfer (LRCT) excited state, and also over precious metal-based phosphorescent materials, which often exhibit similarly broad emission.[9–12] Therefore, the combination of high efficiency and exceptional color purity positions MR-TADF emitters as key candidates for wide-color-gamut displays meeting the stringent BT.2020 standard.[13]

In view of their distinctive merits, most studies on MR-TADF emitters have focused on achieving desired emission colors and high efficiencies through elaborate structure optimizations.[14–16] Extensive molecular design and synthesis approaches through the regulation of boron–nitrogen arrangement modes within MR skeletons, heteroatom modulation, and peripheral decoration with various substituents have proven effective for spectral tuning of MR-TADF emitters across the visible range, enabling full-color devices.[17] Significant advances have been made in the

[a]State Key Laboratory of Integrated Optoelectronics, JLU Region, College of Electronic Science and Engineering, Jilin University, Changchun 130012, P. R. China. E-mail: jinbwei@jlu.edu.cn

[b]State Key Laboratory of Supramolecular Structure and Materials, College of Chemistry, Jilin University, Changchun 130012, P. R. China. E-mail: yuewang@jlu.edu.cn

[c]Institute of Functional Nano and Soft Materials (FUNSOM), Joint International Research Laboratory of Carbon-Based Functional Materials and Devices, Soochow University, Suzhou, Jiangsu, P. R. China. E-mail: xkchen@suda.edu.cn

[d]Department of Chemistry, City University of Hong Kong, Kowloon, Hong Kong SAR, P. R. China

† X. Cai and R. Walia contributed equally to this work.

research on highly efficient MR-TADF-based OLEDs with perfect color purity. These achievements are of great significance for promoting the progress of the organic electroluminescent display industry, and a large number of high-performance MR-TADF materials have been reported.[18–20] However, to establish a more efficient molecular design strategy, a deeper and more precise understanding of the molecular geometry- and chemical-bonding-mode-dependent emission characteristics of MR-TADF molecules remains extremely important. For MR-TADF emitters, it is still a crucial issue to investigate the intrinsic relationship between structures (including molecular geometry and electronic structures) and critical photophysical parameters such as singlet-triplet energy gaps (ΔE_{ST}), excited-state lifetime, reverse intersystem crossing (RISC) rates and FWHM.

In this context, we designed and synthesized a series of MR-TADF molecules with the most basic MR skeletons and devoid of any substituents, which served as a model system to elucidate the structure–property relationships. In our model system, isomeric MR-TADF molecules (Fig. 1) that differ only in their intramolecular bonding modes were constructed and used to elucidate the intramolecular carbon–carbon bonding pattern dependent photophysical properties. The charge transfer excited-state characteristics of MR-TADF molecules are directly governed by the chemical bonding modes within MR frameworks. For a pair of isomers in this study, differences in their emission properties can therefore be attributed to the variation of intramolecular bonding mode. Our approach cleverly eliminates the interference of other factors (such as different substituents, molecular conformation, conjugation degree and so on) on the emission properties of MR-TADF molecules. Therefore, the isomeric MR-TADF molecules provide an ideal platform to dissect how minute structural alterations directly modulate the electronic structures, excited-state and emission characteristics. We anticipate that these insights will significantly deepen the mechanistic understanding of MR-TADF materials and provide essential, fundamental design principles for the future development of organic emitters with predictable and optimized performance.

Results and discussion

To investigate structure–property relationships particularly the effects of bonding connectivity on MR-TADF photophysics, we engineered a series of isomeric mono-boron emitters based on the well-known DABNA-1 prototype.[21] These model molecular isomers share identical molecular formulas but feature distinct C–C bonding connectivity within conserved polycyclic frameworks (Fig. 1). This minimalist approach preserves the MR core while essentially maintaining the spatial arrangement of electron-donating nitrogen and electron-accepting boron atoms. The detailed syntheses and characteristics of the MR-TADF model molecules in this study are presented in the SI (Fig. S1–S10).

DABNA-1 features mutually *para*-positioned B/N atoms, where the MR effect localizes the lowest unoccupied molecular orbital (LUMO) and highest occupied molecular orbital (HOMO) distributions on adjacent atoms. This electronic configuration induces an SRCT excited state that simultaneously minimizes the singlet–triplet energy gaps (ΔE_{ST}) and reduces the reorganization energies, thereby enabling efficient ultra-narrow emission. Consequently, DABNA-1 achieves efficient pure blue emission with a photoluminescence peak at 453 nm, a narrow FWHM of 25 nm, and a high Φ_{PL} exceeding 90% in dilute toluene (10^{-5} M). Derived from the DABNA-1 prototype, the two mono-boron isomers, MR-Cz-1 and MR-Cz-2, retain the basic MR-core framework with only strategic variations in C–C bonding connectivity.[22] Compared to the parent molecule, replacing the diphenylamine moiety with a carbazole unit through the formation of a C–C bond increases the extent of conjugation, which generally facilitates emission bathochromic shifts and is employed to modify the emission maxima of MR-TADF molecules. As a result, the model molecule MR-Cz-2 demonstrates an emission maximum at 469 nm with an FWHM of 23 nm and a distinct absorption band at around 450 nm in the low-energy region, which mirrors its photoluminescence (PL) spectrum and is primarily attributed to its SRCT transition (Fig. 2). Counterintuitively, despite possessing a similar conjugated structure, the isomer MR-Cz-1 exhibits an anomalous hypsochromic shift to 445 nm while maintaining

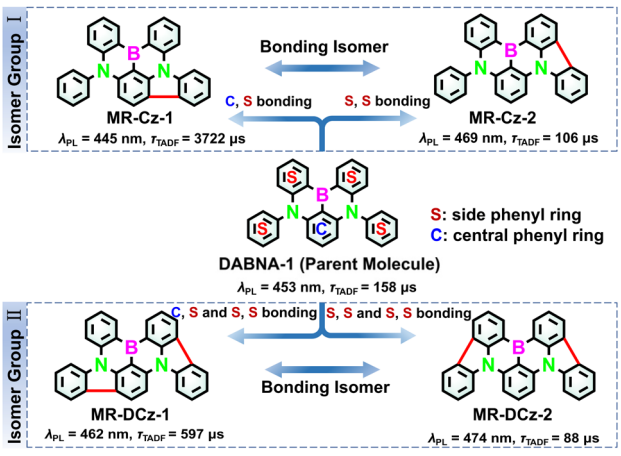

Fig. 1 Chemical structures of the two groups of MR-TADF model molecule isomers.

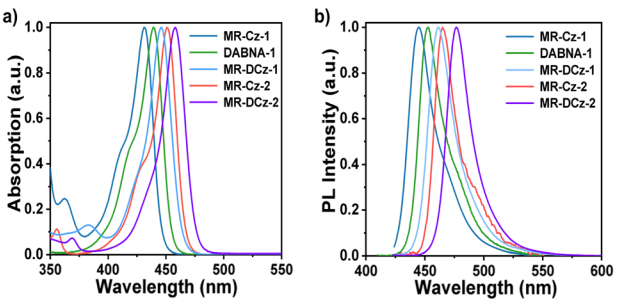

Fig. 2 Normalized (a) UV-vis absorption and (b) PL spectra of DABNA-1, MR-Cz-1/2 and MR-DCz-1/2.

a comparable FWHM. Additionally, the ΔE_{ST} of MR-Cz-1 is 0.25 eV, which is larger than that of MR-Cz-2 (ΔE_{ST} = 0.16 eV). To validate this anomalous observation, we constructed another pair of model isomers with additional C–C bonds in their molecular frameworks. Consistent with this trend, isomer MR-DCz-1 exhibited a blue emission at 462 nm (ΔE_{ST} = 0.21 eV), whereas isomer MR-DCz-2 displayed a bathochromic shift emission to 474 nm with a reduced ΔE_{ST} of 0.14 eV.[23] The detailed photophysical data are summarized in Table 1.

The PL properties in the solid film state were also studied by dispersing these model isomers into 9-(2-(9-phenyl-9*H*-carbazol-3-yl)phenyl)-9*H*-3,9′-bicarbazole (PhCzBCz) with a doping concentration of 1.0 wt%.[24] The emission spectra, FWHMs, and Φ_{PL} s of the doped films closely resemble those in the solution state (Table 2). However, the transient decay curve indicates that MR-Cz-1 suffers from a notably prolonged delayed fluorescence lifetime (τ_{TADF} = 3722 μs) while MR-Cz-2 exhibits a marginally reduced excited-state lifetime of 106 μs relative to that of DABNA-1. Similarly, we also observed distinct differences in another pair of isomers, where MR-DCz-1 exhibited a delayed fluorescence lifetime of 597 μs, whereas MR-DCz-2 showed a comparatively short lifetime of 88 μs. The shortened excited-state lifetime is beneficial for mitigating triplet–triplet annihilation (TTA) and/or triplet-polaron annihilation (TPA) processes, thereby enhancing device efficiency and suppressing efficiency roll-off, which constitutes a pivotal design imperative for advanced MR-TADF emitters (Fig. S37 and Table S1).[25] The photophysical profiles of these isomeric models, which encompass emission spectra and excited-state lifetimes, demonstrate that subtle variations in connectivity drive significant changes in both emission color and exciton dynamics.

To uncover how subtle structural modifications influence their luminescence behavior, we carried out systematic theoretical investigations to establish rational design paradigms for high-performance MR-TADF emitters. The details of all quantum chemistry calculations employed are given in the SI Section "Computational Methodology". As a starting point, the simplest excited-state method, configuration interaction singles (CIS), was applied to five representative model molecules shown in Fig. 1. The CIS method is the excited-state analogue of the Hartree–Fock method and includes little electron-correlation effects in excited states. As shown in Fig. 3a, the CIS-calculated S_1 energies (E_{S1}[CIS]) show poor agreement with experimental values (E_{S1}[Exp]) and the absence of correlation effects not only leads to overestimation of absolute excitation energies but also fails to reproduce the red-shifted emission trend among these five molecules (Table S2).

To account for electron correlation effects, we employed the high-level coupled-cluster (CC) approach, specifically the STEOM-DLPNO-CCSD method, to compute the excited-state energies of the same molecular set. The CC-calculated S_1 energies (E_{S1}[CC]) are in good agreement with experimental results (Fig. 3b), both in absolute values and in reproducing the observed red-shifted trend (Table S2). These results confirm that the inclusion of electron correlation effect is essential to accurately describe the S_1 energetics and photophysical behavior of MR-TADF systems, as previously established in our work and by others.[26–28] The CC-based ΔE_{S1T1} values were also evaluated to be 0.36, 0.19, 0.30, 0.24, and 0.19 eV for MR-Cz-1, DABNA-1, MR-DCz-1, MR-Cz-2, and MR-DCz-2, respectively (Table S2). For comparison, we also calculated the excited-state energies and ΔE_{ST} values at the B3LYP/6-31G(d, p) level, the results are summarized in Table S3.

To further probe the molecular origin of the emission shifts in detail, we decomposed S_1 energies to the two parts such as: E_{S1}[Ints] estimated *via* a two-electron two-orbital model without inclusion of electron correlation effects, and the electron-correlation contribution E_{S1}[Corr] defined as the difference between E_{S1}[CIS] and E_{S1}[CC] (see SI Section "Computational Methodology"). Adding E_{S1}[Corr] to E_{S1}[Ints] yields a corrected S_1 energy incorporating both contributions, denoted as E_{S1}[Ints + Corr]. Similar to the CIS results, E_{S1}[Ints] values show poor agreement with experiment and fail to reproduce the emission-energy trend across the five model molecules (Fig. 3c). In contrast, E_{S1}[Ints + Corr] values exhibit excellent agreement, with a Pearson correlation coefficient ~1 and all points lying close to the best-fit line (Fig. 3d), this highlights the critical role of electron correlation in shaping the emission behavior of MR-TADF systems. Compared to DABNA-1 (E_{S1}[Corr] = −1.67 eV), MR-Cz-1 exhibits slightly weaker correlation (E_{S1}[Corr] = −1.57 eV). Notably, E_{S1}[Ints] values for MR-Cz-1 and DABNA-1 are 5.33 and 5.35 eV, respectively (opposite to the trends observed experimentally and CC-calculated theoretically), whereas E_{S1}[Ints + Corr] values are 3.77 and 3.68 eV, correctly reproducing

Table 1 Summary of the physical properties of mono-boron mode molecules in solution

Compound	λ_{abs} [a] [nm]	λ_{em} [b] [nm]	FWHM [c] [nm/eV]	E_{S1} [d] [eV]	E_{T1} [e] [eV]	ΔE_{ST} [f] [eV]	E_g [g] [eV]	HOMO [h] [eV]	LUMO [h] [eV]	Φ_{PL} [i] [%]
MR-Cz-1	431	445	25/0.16	2.88	2.63	0.25	2.86	−5.21	−2.35	92
DABNA-1	439	453	25/0.15	2.82	2.63	0.19	2.72	−5.08	−2.36	91
MR-DCz-1	446	462	25/0.15	2.76	2.55	0.21	2.70	−5.23	−2.53	92
MR-Cz-2	450	469	23/0.13	2.74	2.60	0.16	2.65	−5.18	−2.53	93
MR-DCz-2	457	474	24/0.13	2.69	2.56	0.14	2.61	−5.33	−2.72	91

[a] Peak wavelength of the lowest energy absorption band. [b] Peak wavelength of the PL spectrum in toluene solution (1×10^{-5} M, 298 K). [c] Full-width at half-maximum. [d] Singlet energy estimated from the onset of the fluorescence spectrum in toluene solution (1×10^{-5} M, 77 K). [e] Triplet energy estimated from the onset of the phosphorescence spectrum in a frozen toluene matrix (1×10^{-5} M, 77 K). [f] $\Delta E_{ST} = E_{S1} - E_{T1}$. [g] Optical band gap estimated from the absorption edge of the UV-vis spectrum. [h] Determined from cyclic voltammetry using the formula: $E_{HOMO} = -(E_{ox} + 4.8)$ eV and $E_{LUMO} = -(E_{red} + 4.8)$ eV. [i] Absolute photoluminescence quantum yield measured with an integrating sphere in N_2-bubbling toluene solution (1×10^{-5} M, 298 K).

Table 2 Summary of photophysical data of 1 wt% template compounds in PhCzBCz doped films

Emitter	λ_{em}[a] [nm]	FWHM[b] [nm/eV]	Φ_{PL}[c] [%]	Φ_F[d] [%]	Φ_{TADF}[e] [%]	τ_F[f] [ns]	τ_{TADF}[g] [μs]	k_r[h] [10^7 s^{-1}]	k_{nr}[i] [10^6 s^{-1}]	k_{ISC}[j] [10^7 s^{-1}]	k_{RISC}[k] [10^3 s^{-1}]
MR-Cz-1	451	32/0.19	91	69	22	9.0	3722	7.7	7.6	2.7	0.4
DABNA-1	460	27/0.16	90	79	11	8.4	158	9.3	10.3	1.5	7.3
MR-DCz-1	468	33/0.19	90	66	24	6.9	597	9.6	10.6	3.8	2.3
MR-Cz-2	473	29/0.16	92	76	16	7.6	106	10.0	8.7	2.2	11.4
MR-DCz-2	483	31/0.17	91	74	17	6.6	88	11.1	11.0	2.9	14.1

[a] PL emission maximum. [b] Full width at half maximum of the PL spectrum. [c] The total photoluminescence quantum yield (Φ_{PL}). [d] The prompt fluorescent (Φ_F) component of Φ_{PL}. [e] The delayed fluorescent (Φ_{TADF}) component of Φ_{PL}. [f] The lifetime of prompt fluorescence (τ_F). [g] The lifetime of delayed fluorescence (τ_{TADF}). [h] The rate constant of radiative decay (k_r). [i] The rate constant of non-radiative decay (k_{nr}). [j] The rate constant of intersystem crossing (k_{ISC}). [k] The rate constant of reverse intersystem crossing (k_{RISC}).

the experimental and CC-calculated trend. These results on DABNA-1 and MR-Cz-1 demonstrate that the hypsochromic shift is primarily driven by electron-correlation effects (Table S4). Difference density analysis (Fig. 3e) shows that in MR-Cz-1, electron density delocalizes over the extended framework arising from the additional C–C connectivity (solid black circle). However, this delocalization lacks the alternating electron-rich/electron-deficient pattern characteristic of MR systems, resulting in weaker correlation stabilization. Based on Mulliken-partition atomic contribution analysis of the frontier molecular orbitals, the weaker correlation in MR-Cz-1 can be attributed to the loss of orbital symmetry induced by the additional C–C connectivity, which disrupts the balanced delocalization of the HOMO across the two nitrogen atoms (Fig. S38 and S39). In DABNA-1, both N atoms contribute equally (9.2% each) to the HOMO, maintaining the symmetry that supports effective resonance and strong configuration mixing. However, in MR-Cz-1, one N atom contributes 9.9% while the other contributes only 2.6%, indicating localization and broken orbital symmetry. Although the two N-atoms contribute less to the LUMO overall, this asymmetry is also reflected there, with the two N atoms contributing 2.1% and 0.7%, respectively (Fig. S39). Consequently, the CC-calculated S_1 energy for MR-Cz-1 (2.97 eV) is slightly higher than DABNA-1 (2.94 eV), explaining the observed hypsochromic shift.

In MR-Cz-2, the extended framework retains the MR character, and despite the additional C–C connectivity, the two N atoms contribute almost equally to the HOMO (8.3% and 9.2%), indicating only slight disruption to orbital symmetry (Fig. S39). Consequently, the electron correlation contribution (E_{S1}[Corr] = −1.64 eV, as shown in Fig. 3e) is only slightly affected relative to DABNA-1 (E_{S1}[Corr] = −1.67 eV). The E_{S1}[Ints] value of 5.22 eV in MR-Cz-2 is slightly smaller than DABNA-1 (5.35 eV), thus explaining the experimental bathochromic trend. Therefore, E_{S1}[Ints + Corr] values (3.58 for MR-Cz-2 *vs.* 3.68 eV for DABNA-1) also follow the correct trend. Similarly, in the case of MR-DCz-1 and MR-DCz-2, both molecules have similar E_{S1}[Ints] of 5.15 and 5.14 eV, respectively (Table S4), but the correlation contributions E_{S1}[Corr] differ significantly due to MR effects, *i.e.*, −1.55 eV for MR-DCz-1 *versus* −1.63 eV for MR-DCz-2 (Fig. 3e). This difference also arises from the broken orbital symmetry of the molecular orbitals in MR-DCz-1, whereas the symmetry is largely preserved in MR-DCz-2 (Fig. S39). Thus, the larger correlation stabilization in MR-DCz-2 lowers E_{S1}[Ints + Corr] to 3.51 eV compared to 3.59 eV in MR-DCz-1, explaining the red-shifted emission and confirming that the distinct electron correlation effect dominates the emission shift in these extended systems.

Having established that the bonding connectivity pattern fundamentally governs the photophysical properties of mono-boron MR-TADF isomers, we next probed whether these structure-emission relationships extend to more complex multi-resonant architectures. To validate the universality of bonding connectivity-governed exciton control, we engineered dual-boron isomers that conserve the core resonance topology while introducing strategic boron positioning differences. This progression enables the rigorous testing of our mechanistic model, which posits that atomic connectivity directly modulates frontier orbital interactions and associated excited-state dynamics, independent of peripheral modifications.

As illustrated in Fig. 4a, these dual-boron isomers were derived from the classical *ν*-DABNA architecture while preserving the mono-boron core framework.[29] Benefiting from a one-pot double tandem lithiation–borylation–annulation reaction, several MR emitters featuring *meta*-B/*para*-B connectivity isomers were designed and synthesized (Schemes S2–S5 and Fig. S11–S29). All these emitters exhibit a sharp absorption band and high Φ_{PL}s (93–96%) in dilute toluene (10^{-5} M) (Fig. 4b–c and Table S5). Compared with DABNA-1, *ν*-DABNA features a more rigid scaffold with enhanced electronic confinement that intensifies the MR effect, inducing a bathochromic shift in emission to 466 nm and achieving an ultra-narrow FWHM of 16 nm. As reported by Kwon *et al.*, Cz-DBMR exhibits a sky-blue emission peak at 477 nm with an identical FWHM.[30] This double B/N configuration extends the resonance effect beyond the MR-Cz-2 motif, enabling stronger orbital overlap and suppressed vibrational relaxation. Crucially, covalent integration of diphenylamine at the central benzene core in isomer *ν*-DABNA-Cz parallels the structural strategy in MR-Cz-1, triggering an identical hypsochromic shift mechanism toward deep-blue emission (λ = 448 nm) while preserving an ultra-narrow FWHM of 16 nm, which is a critical requirement for BT.2020 compliance. In contrast, *g*-DABNA—the *para*-boron isomer of *ν*-DABNA exhibits significantly redshifted emission at 539 nm (yellow-green region) with a modestly broadened FWHM of 23 nm and a moderate singlet-triplet energy gap (ΔE_{ST} = 0.19 eV) due to the enhanced delocalized

excited states and reinforced structural rigidity. These minor structural modifications facilitate considerable bathochromic shifts (>70 nm), thereby enabling the realization of long-wavelength emission in the targeted MR-TADF emitters.[1,4,31] Similarly, compound *g*-DABNA-Cz exhibits a blue-green emission peak at 495 nm with an FWHM of 21 nm, demonstrating a hypsochromic shift relative to *g*-DABNA. These results further validate the structure–property correlation established in mono-boron model systems. Guided by these findings, we designed and synthesized an asymmetric double-boron MR-TADF emitter with ultra-pure green emission (*x*-DABNA-Cz, λ = 520 nm, FWHM = 24 nm), where the asymmetric B/N topology selectively enhances long-range charge transfer while maintaining a rigid core for narrowband emission, establishing it as a critical component for wide color-gamut displays. Furthermore, based on the low-temperature fluorescence (77 K) and phosphorescence spectra (Fig. S42), the ΔE_{ST}s were calculated to be 0.04, 0.02, 0.22, 0.19, 0.14, and 0.17 eV for *ν*-DABNA, Cz-DBMR, *ν*-DABNA-Cz, *g*-DABNA, *g*-DABNA-Cz, and *x*-DABNA, respectively (Table S4).

We further measured the solid-state PL properties by dispersing these emitters (1.0 wt%) into PhCzBCz. As shown in Fig. S43 and Table S6, all of the blend films maintained high Φ_{PL} values of 96–98% with emission maxima of 470 nm (*ν*-DABNA), 484 nm (Cz-DBMR), 452 nm (*ν*-DABNA-Cz), 542 nm (*g*-DABNA), 497 nm (*g*-DABNA-Cz), and 521 nm (*x*-DABNA),

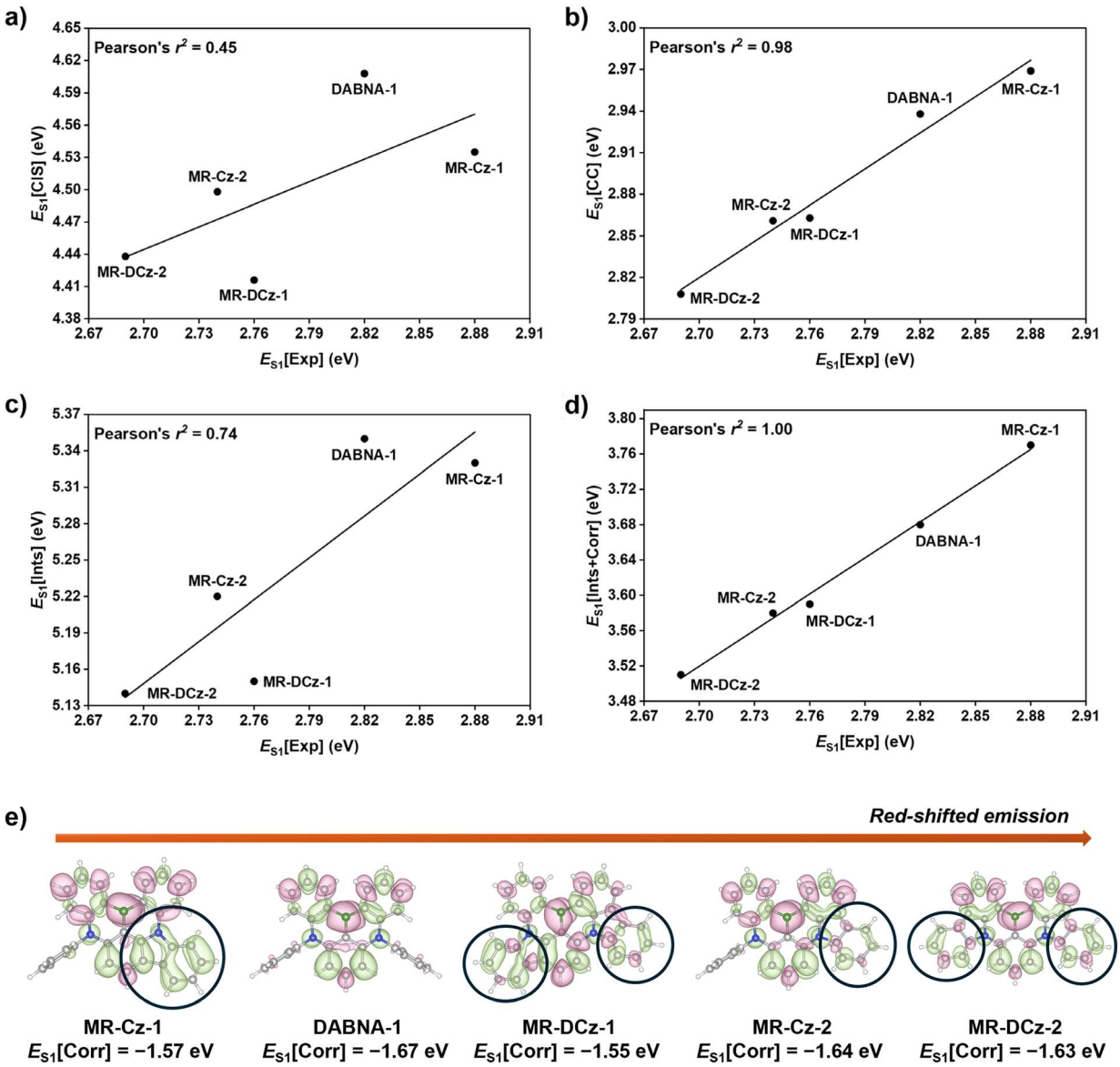

Fig. 3 Quantum chemical analysis of MR-TADF model isomers. (a) Experimentally measured S_1 energies (E_{S1}[Exp]) plotted against CIS-calculated S_1 energies (E_{S1}[CIS]). (b) E_{S1}[Exp] *versus* CC-calculated S_1 energies (E_{S1}[CC]). E_{S1}[Exp] plotted against S_1 energies evaluated from (c) E_{S1}[Ints] *via* a two-electron two-orbital model and (d) E_{S1}[Ints + Corr] from the combined effects of integrals and correlation effects. (e) CC-based difference density analysis at isosurface level of 5×10^{-4} a.u. for five model molecules, with corresponding electron correlation contribution (E_{S1}[Corr]) to the S_1 state. Green and red densities represent regions of increased and decreased electron density, respectively, during the electronic excitation. The detailed values of all parameters are provided in SI Tables S2 and S4.

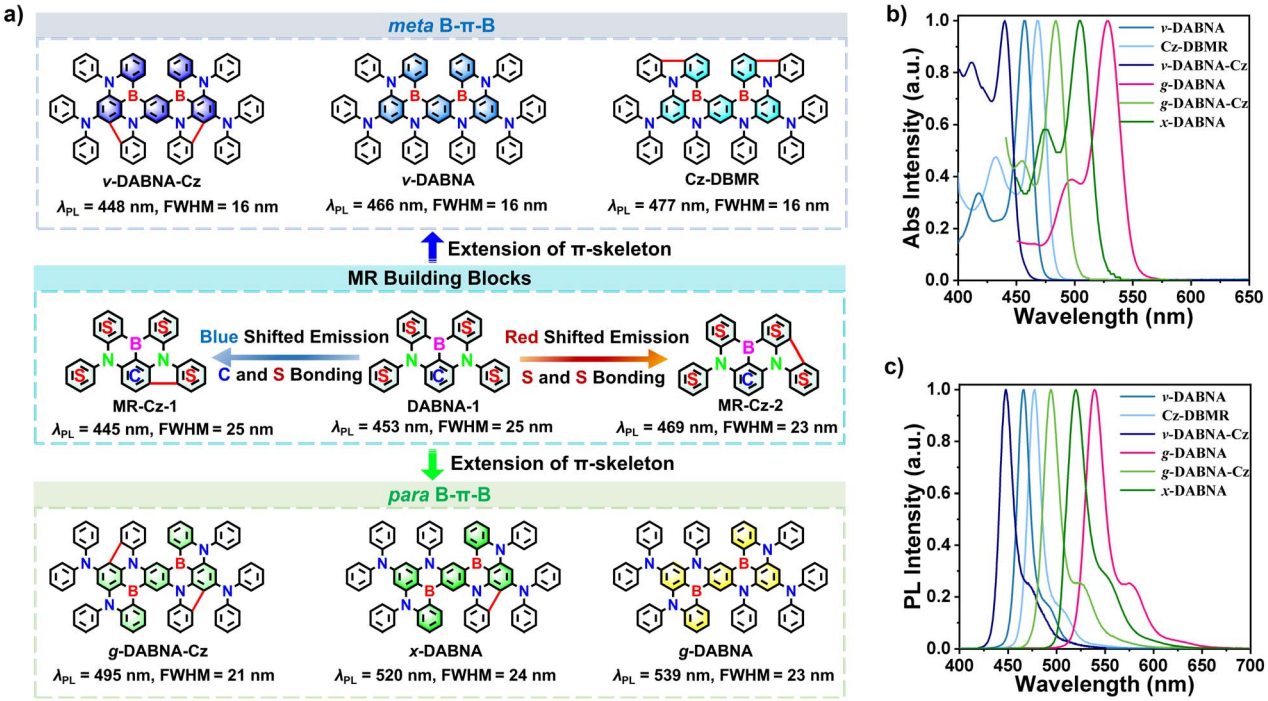

Fig. 4 Molecular structures (a), normalized UV-vis absorption (b), and PL spectra (c) of *ν*-DABNA, Cz-DBMR, *ν*-DABNA-Cz, *g*-DABNA, *g*-DABNA-Cz, and *x*-DABNA.

exhibiting slight bathochromic shifts relative to their solution-state values. Besides, these materials maintain narrow emission bandwidths (FWHM: 18–28 nm) in the solid state, exhibiting only minimal broadening compared to those in the solution state. The transient decay curves of *ν*-DABNA, Cz-DBMR, *ν*-DABNA-Cz, *g*-DABNA, *g*-DABNA-Cz and *x*-DABNA showed two components, corresponding to prompt lifetimes of 8.6, 7.2, 3.3, 7.4, 7.2 and 8.7 ns, respectively, and delayed lifetimes of 3.0, 2.5, 234.2, 1392.4, 82.3, and 2950.1 μs, respectively (Fig. S44–S45). These minor structural modifications induce consistent alterations in photophysical behaviors such as emission maxima and excited-state lifetimes, demonstrating that the results align with structure–property relationships established in monomeric B/N model compounds.

Compounds *ν*-DABNA-Cz and *x*-DABNA exhibit high Φ_{PL} values, narrow FWHMs, and efficient TADF characteristics, indicating their promise as deep-blue and green emitters for highly efficient OLEDs with superior color purity, respectively. The electroluminescence performance was further evaluated using an OLED structure of [ITO/TAPC (45 nm)/TCTA (5 nm)/MCP (5 nm)/emission layer (EML, 30 nm)/DPEPO (5 nm)/TmPyPb (30 nm)/LiF (1 nm)/Al (100 nm)]. The detailed device structure with the energy levels of the corresponding materials is illustrated in Fig. 5a, while the molecular structures of the materials are shown in Fig. 5b. Here, 1,1-Bis(4-di-*p*-tolylaminophenyl)cyclohexane (TAPC) served as the hole transport layer (HTL), 1,3,5-tri[(3-pyridyl)-phen-3-yl] benzene (TmPyPb) served as the electron transport layer (ETL), and LiF served as the electron injection layer (EIL). Additionally, 4,4′,4″-tris(carbazol-9-yl)-triphenylamine (TCTA), 1,3-di(9*H*-carbazol-9-yl)benzene (MCP) and Bis[2-(diphenylphosphino)phenyl] ether oxide (DPEPO) functioned as exciton blocking layers due to their well-matched energy levels and high triplet energy, effectively confining excitons within the EML.

The EMLs, which consisted of PhCzBCz:1 wt% *ν*-DABNA-Cz (device A) and *x*-DABNA (device B), were constructed. As depicted in Fig. 5c and summarized in Table 3, devices A and B displayed narrowband EL emissions with peaks at 451 and 522 nm, accompanied by narrow FWHMs of 0.11 and 0.12 eV, respectively. Encouragingly, the corresponding devices achieved CIE coordinates of (0.138, 0.057) and (0.208, 0.724), meeting the NTSC standard while converging notably toward the BT.2020 color gamut.[32] Furthermore, devices A and B showed impressively high EQE values of 32.0% and 29.9%, respectively. However, the prolonged delayed fluorescence lifetimes of *ν*-DABNA-Cz and *x*-DABNA exacerbate severe bimolecular quenching at elevated current densities, leading to significant efficiency roll-off and limiting their practical utility.

To enhance exciton utilization and suppress efficiency roll-off, sensitization strategies were employed to achieve efficient exciton harvesting.[33,34] Specifically, m-4TCzPhBN and $Ir(ppy)_3$ were selected as sensitizers for *ν*-DABNA-Cz and *x*-DABNA, respectively, because of the significant spectral overlap between the sensitizers' emission and the emitters' absorption spectra, which enables high-efficiency energy transfer (Fig. S48–S50).[35,36] The corresponding device structure was optimized with the following EMLs: PhCzBCz:25 wt% m-4TCzPhBN : 1 wt% *ν*-DABNA-Cz (device C), and PhCzBCz:25 wt% $Ir(ppy)_3$: 1 wt% *x*-DABNA (device D). As shown in Fig. 5c–**e**, the sensitized OLEDs exhibited narrowband electroluminescence at 451 nm (FWHM

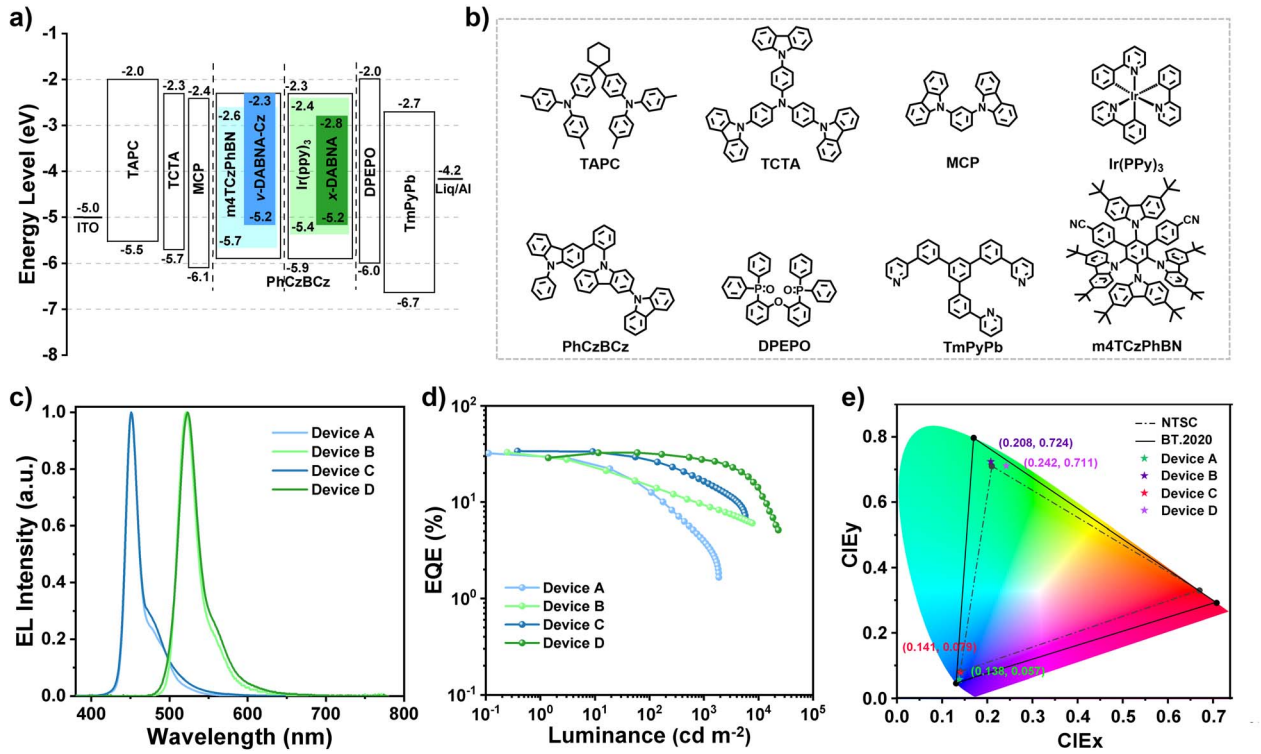

Fig. 5 EL characteristics of OLED devices fabricated with *ν*-DABNA-Cz and *x*-DABNA. (a) Device structure with energy level diagram. (b) Molecular structures of the materials used in the devices. (c) Normalized EL spectra of device A–D. (d) EQE *versus* luminance. (e) CIE (*x*, *y*) coordinate.

Table 3 Summary of the EL data of the *ν*-DABNA-Cz and *x*-DABNA-based devices

Device	λ_{em}[a] [nm]	FWHM[b] [nm/eV]	V_{on}[c] [V]	L_{max}[d] [cd m^{-2}]	CE_{max}[e] [cd A^{-1}]	PE_{max}[f] [lm W^{-1}]	EQE[g] [%]	CIE[h] (*x*, *y*)
Device A	451	19/0.11	3.3	1874	20.4	21.4	32.0/12.9/3.9	(0.138, 0.057)
Device B	522	28/0.12	3.2	7724	118.5	115.4	29.9/14.6/9.1	(0.208, 0.724)
Device C	451	19/0.11	3.1	5825	30.3	31.7	33.8/27.1/16.2	(0.141, 0.079)
Device D	524	29/0.12	3.1	23 092	123.9	114.4	32.5/31.9/27.4	(0.242, 0.711)

[a] EL peak wavelength at 100 cd m^{-2}. [b] Full width at half maximum of the spectra given in wavelength. [c] Turn-on voltage at 1 cd m^{-2}. [d] Maximum luminance. [e] Maximum current efficiency. [f] Maximum power efficiency. [g] Maximum external quantum efficiency, and values at 100 and 1000 cd m^{-2}, respectively. [h] Value taken at 100 cd m^{-2}.

= 0.11 eV) and 524 nm (FWHM = 0.12 eV), with CIE coordinates of (0.14, 0.08) for *ν*-DABNA-Cz and (0.24, 0.71) for *x*-DABNA, respectively. Additionally, the sensitized device demonstrated excellent spectral stability over a broad driving voltage range from 3.5 to 9.5 V, indicating an efficient energy transfer process (Fig. S51). In addition to the superior emission spectra, these devices achieved maximum EQEs of 33.8% (device C) and 32.5% (device D), with corresponding current efficiencies (CEs) of 30.3 cd A^{-1} and 123.9 cd A^{-1}, and power efficiencies (PEs) of 31.7 lm W^{-1} and 114.4 lm W^{-1}, respectively. Moreover, the efficiency roll-off was significantly suppressed at 1000 cd m^{-2}, retaining EQEs of 16.2% (device C) and 27.4% (device D), which is attributed to the efficient exciton recycling and energy transfer processes in ternary-doped emissive layers. Moreover, we also evaluated the operational stability of sensitizer-based devices employing a stable device architecture (Fig. S52a). Following a previously reported method, the operational lifetime, LT50 (defined as the time at which the luminance decreases to 50% of its initial value), was estimated using an acceleration factor (*n*) of 1.7.[16] Correspondingly, the extrapolated LT50 values at an initial luminance of 1000 cd m^{-2} were 1033 and 2106 h for *ν*-DABNA-Cz and *x*-DABNA-based devices, respectively (Fig. S52b).

Conclusions

By investigating model molecules with isomeric bonding motifs, this study provides insight into the structure–property relationships of MR-TADF emitters. Bonding between the central phenyl ring (C ring) and a side phenyl ring (S ring) induces a hypsochromic emission shift, whereas bonding between two S rings leads to a bathochromic emission shift; this trend is consistent across both mono- and dual-boron systems.

Notably, C–S bonding results in remarkably long delayed lifetimes, reflecting a significant increase in ΔE_{ST}. Theoretical analyses reveal that C–S bonding disrupts the alternating electron-rich/electron-deficient resonance pattern, thereby weakening electron correlation and raising the S_1 energy, which gives rise to a hypsochromic shift. In contrast, S–S bonding preserves or reinforces this pattern, enhancing correlation stabilization and leading to a bathochromic shift. Moreover, both experimental and theoretical results indicate that emission shifts are not governed solely by electron correlation; in specific cases, variations in one- and two-electron integral contributions also play decisive roles. These findings demonstrate that bonding connectivity fundamentally governs photophysical properties of MR-TADF emitters and provides a rational basis for molecular design. The deep-blue and pure-green emitters developed in this work further validate the effectiveness of this design strategy.

Author contributions

Xinliang Cai and Yexuan Pu performed the molecular synthesis, photophysical measurements, and device characterization. Rajat Walia and Weixiong Guo carried out the theoretical calculations and analysis under the supervision of Xian-Kai Chen. Jinbei Wei, Xian-Kai Chen, and Yue Wang conceived the project, supervised the research, and contributed to manuscript preparation. All authors discussed the results and contributed to the final manuscript.

Conflicts of interest

There are no conflicts to declare.

Data availability

All data supporting this study are included in the article and its supplementary information (SI). Supplementary information is available. See DOI: https://doi.org/10.1039/d6sc02775j.

Acknowledgements

This work was supported by the National Natural Science Foundation of China (523B2031, 52303230), the Jilin Provincial Science and Technology Development Plan Project (20250101023JJ), and the Postdoctoral Fellowship Program of CPSF (GZB20250229). X.-K. Chen also acknowledges the financial support from the National Natural Science Foundation of China (52473190), the Natural Science Foundation of Jiangsu Province (BK20240042), the Science and Technology Project of Suzhou (ZXL2024394), the Suzhou Key Laboratory of Functional Nano & Soft Materials, Collaborative Innovation Center of Suzhou Nano Science & Technology, and the 111 Project. R. Walia sincerely thanks the Jiangsu Province Excellent Postdoctoral Program (2024ZB898) for the financial support.

Notes and references

1 M. Yang, I. S. Park and T. Yasuda, *J. Am. Chem. Soc.*, 2020, **142**, 19468.
2 N. Ikeda, S. Oda, R. Matsumoto, M. Yoshioka, D. Fukushima, K. Yoshiura, N. Yasuda and T. Hatakeyama, *Adv. Mater.*, 2020, **32**, 2004072.
3 Y. Xu, C. Li, Z. Li, Q. Wang, X. Cai, J. Wei and Y. Wang, *Angew. Chem., Int. Ed.*, 2020, **59**, 17442.
4 Y. Zou, J. Hu, M. Yu, J. Miao, Z. Xie, Y. Qiu, X. Cao and C. Yang, *Adv. Mater.*, 2022, **34**, 2201442.
5 J. Park, K. J. Kim, J. Lim, T. Kim and J. Y. Lee, *Adv. Mater.*, 2022, **34**, 2108581.
6 H.-Z. Li, F.-M. Xie, Y.-Q. Li and J.-X. Tang, *J. Mater. Chem. C*, 2023, **11**, 6471.
7 H. Jiang, J. Jin and W.-Y. Wong, *Adv. Funct. Mater.*, 2023, **33**, 2306880.
8 X. Wu, S. Ni, C.-H. Wang, W. Zhu and P.-T. Chou, *Chem. Rev.*, 2025, **125**, 6685.
9 H. Uoyama, K. Goushi, K. Shizu, H. Nomura and C. Adachi, *Nature*, 2012, **492**, 234.
10 Y. Im, M. Kim, Y. J. Cho, J.-A. Seo, K. S. Yook and J. Y. Lee, *Chem. Mater.*, 2017, **29**, 1946.
11 J. Sun, H. Ahn, S. Kang, S.-B. Ko, D. Song, H. A. Um, S. Kim, Y. Lee, P. Jeon, S.-H. Hwang, Y. You, C. Chu and S. Kim, *Nat. Photonics*, 2022, **16**, 212.
12 M.-C. Tang, M.-Y. Chan and V. W.-W. Yam, *Chem. Rev.*, 2021, **121**, 7249.
13 X. Fan, X. Hao, F. Huang, J. Yu, K. Wang and X. Zhang, *Adv. Sci.*, 2023, **10**, 2303504.
14 T. Fan, Y. Zhang, L. Wang, Q. Wang, C. Yin, M. Du, X. Jia, G. Li and L. Duan, *Angew. Chem., Int. Ed.*, 2022, **61**, e202213585.
15 S. Uemura, S. Oda, M. Hayakawa, R. Kawasumi, N. Ikeda, Y.-T. Lee, C.-Y. Chan, Y. Tsuchiya, C. Adachi and T. Hatakeyama, *J. Am. Chem. Soc.*, 2023, **145**, 1505.
16 X. Cai, Y. Xu, Y. Pan, L. Li, Y. Pu, X. Zhuang, C. Li and Y. Wang, *Angew. Chem., Int. Ed.*, 2023, **62**, e202216473.
17 M. Mamada, M. Hayakawa, J. Ochi and T. Hatakeyama, *Chem. Soc. Rev.*, 2024, **53**, 1624.
18 J. Liu, Y. Zhu, T. Tsuboi, C. Deng, W. Lou, D. Wang, T. Liu and Q. Zhang, *Nat. Commun.*, 2022, **13**, 4876.
19 H.-J. Cheon, S.-J. Woo, S.-H. Baek, J.-H. Lee and Y.-H. Kim, *Adv. Mater.*, 2022, **34**, 2207416.
20 X.-C. Fan, K. Wang, Y.-Z. Shi, Y.-C. Cheng, Y.-T. Lee, J. Yu, X.-K. Chen, C. Adachi and X.-H. Zhang, *Nat. Photonics*, 2023, **17**, 280.
21 T. Hatakeyama, K. Shiren, K. Nakajima, S. Nomura, S. Nakatsuka, K. Kinoshita, J. Ni, Y. Ono and T. Ikuta, *Adv. Mater.*, 2016, **28**, 2777.
22 Y. Qiu, H. Xia, J. Miao, Z. Huang, N. Li, X. Cao, J. Han, C. Zhou, C. Zhong and C. Yang, *ACS Appl. Mater. Interfaces*, 2021, **13**, 59035.
23 Y.-T. Lee, C.-Y. Chan, M. Tanaka, M. Mamada, U. Balijapalli, Y. Tsuchiya, H. Nakanotani, T. Hatakeyama and C. Adachi, *Adv. Electron. Mater.*, 2021, **7**, 2001090.

24 Y. Xu, C. Li, Z. Li, J. Wang, J. Xue, Q. Wang, X. Cai and Y. Wang, *CCS Chem.*, 2022, **4**, 2065.
25 K. R. Naveen, P. Palanisamy, M. Y. Chae and J. H. Kwon, *Chem. Commun.*, 2023, **59**, 3685.
26 R. Walia, X. Xiong, X.-C. Fan, T.-F. Chen, H. Wang, K. Wang, Y.-Z. Shi, X. Tang, J.-L. Bredas, C. Adachi, X.-K. Chen and X.-H. Zhang, *Nat. Mater.*, 2025, **24**, 1576.
27 A. Pershin, D. Hall, V. Lemaur, J.-C. Sancho-Garcia, L. Muccioli, E. Zysman-Colman, D. Beljonne and Y. Olivier, *Nat. Commun.*, 2019, **10**, 597.
28 D. Hall, J. C. Sancho-García, A. Pershin, G. Ricci, D. Beljonne, E. Zysman-Colman and Y. Olivier, *J. Chem. Theory Comput.*, 2022, **18**, 4903.
29 Y. Kondo, K. Yoshiura, S. Kitera, H. Nishi, S. Oda, H. Gotoh, Y. Sasada, M. Yanai and T. Hatakeyama, *Nat. Photonics*, 2019, **13**, 678.
30 K. R. Naveen, J. H. Oh, H. S. Lee and J. H. Kwon, *Angew. Chem., Int. Ed.*, 2023, **62**, e202306768.
31 Y. Zhang, D. Zhang, T. Huang, A. J. Gillett, Y. Liu, D. Hu, L. Cui, Z. Bin, G. Li, J. Wei and L. Duan, *Angew. Chem., Int. Ed.*, 2021, **60**, 20498.
32 R. M. Soneira, *Inform. Display*, 2016, **32**, 26.
33 C.-Y. Chan, M. Tanaka, Y.-T. Lee, Y.-W. Wong, H. Nakanotani, T. Hatakeyama and C. Adachi, *Nat. Photonics*, 2021, **15**, 203.
34 E. Kim, J. Park, M. Jun, H. Shin, J. Baek, T. Kim, S. Kim, J. Lee, H. Ahn, J. Sun, S.-B. Ko, S.-H. Hwang, J. Y. Lee, C. Chu and S. Kim, *Sci. Adv.*, 2022, **8**, eabq1641.
35 D. Zhang, X. Song, A. J. Gillett, B. H. Drummond, S. T. E. Jones, G. Li, H. He, M. Cai, D. Credgington and L. Duan, *Adv. Mater.*, 2020, **32**, 1908355.
36 X. Cai, Y. Pu, C. Li, Z. Wang and Y. Wang, *Angew. Chem., Int. Ed.*, 2023, **62**, e202304104.